Environmental Science and Ecotechnology 28 (2025) 100639

Contents lists available at ScienceDirect

Environmental Science and Ecotechnology

journal homepage: www.journals.elsevier.com/environmental-science-and-ecotechnology/

Original Research

Oxygen doping enhances piezo-photocatalytic degradation of carbamazepine by molybdenum disulfide

Yanjiao Li [a,b], Lianfeng Wang [a], Yuting Ning [c], Ying Yuan [b], Xinping Fu [c], Jun Cui [c,*], Yu Jiang [b,**]

[a] School of Materials Science and Engineering, Dalian Jiaotong University, Dalian, 116028, China
[b] State Key Laboratory of Environmental Criteria and Risk Assessment, and Key Laboratory of Groundwater Pollution Simulation and Control of Ministry of Ecology and Environment, Chinese Research Academy of Environmental Sciences, Beijing, 100012, China
[c] College of Chemical Engineering, Beijing University of Chemical Technology, Beijing, 100029, China

ARTICLE INFO

Article history:
Received 16 May 2025
Received in revised form
2 December 2025
Accepted 2 December 2025

Keywords:
Piezo-photocatalysis
Oxygen-doped molybdenum disulfide
Piezoelectric properties
Environmental remediation

ABSTRACT

Environmental pollution from persistent pharmaceuticals like carbamazepine (CBZ) poses severe risks to aquatic ecosystems and human health, yet conventional treatments struggle with low concentrations and secondary pollution. Piezo-photocatalysis, which harnesses mechanical and solar energies to drive charge separation, offers a promising alternative using materials such as molybdenum disulfide (MoS_2), whose layered structure enables tunable piezoelectricity but is hindered by rapid electron-hole recombination and structural instability. However, the mechanistic role of oxygen doping in repairing sulfur vacancies and enhancing symmetry-breaking for improved performance remains underexplored. Here we show that hydrothermally synthesized oxygen-doped MoS_2 (O_5-MoS_2) fully degrades 2 mg L^{-1} CBZ in 25 min under combined ultrasound and visible light, achieving a rate constant (k_{obs}) of 0.13 min^{-1}—11.4 times higher than undoped MoS_2. This stems from oxygen substitution narrowing the bandgap to 1.94 eV, boosting the piezoelectric coefficient to 63 p.m. V^{-1} (versus 26 p.m. V^{-1}), and generating a 0.19 V built-in potential that drives charge separation, as confirmed by 4.18 μA cm^{-2} synergistic photocurrents, density functional theory calculations revealing heightened Mo–O charge transfer (2.08–2.36 e^-), and finite element simulations of deformation-induced fields. Over five cycles, O_5-MoS_2 retains 100% efficiency with minimal Mo leaching (1.9%), reducing product toxicity across fish, daphnid, and algal models. These findings delineate oxygen doping's dual role in defect mitigation and polarization enhancement, paving the way for robust piezo-photocatalytic systems in real-world water purification.

1. Introduction

With the rapid development of global industrialization and urbanization, environmental pollution is becoming increasingly severe [1,2]. Water bodies face a serious, hidden threat from the steady increase in organic pollutants, endangering ecosystems and human well-being [3,4]. Carbamazepine (CBZ), a widely used antiepileptic and analgesic agent, is characterized by low concentrations and difficulty in degrading in the environment [5,6]. Low-concentration CBZ not only causes toxic stress to aquatic organisms but may also trigger health crises such as endocrine disorders and increased drug resistance in humans through the food chain [7]. Traditional biological degradation and physical treatment technologies are plagued by low treatment efficiency, high energy consumption, and secondary pollution when treating low-level CBZ pollution [8–10]. These problems make it difficult to meet actual demands.

Currently, environmental remediation research is focused on piezo-photocatalytic technology [11–13]. Before delving into this technology in depth, it is necessary to briefly review the limitations of photocatalysis and piezocatalysis. On the one hand, although photocatalytic technology can utilize solar energy to drive reactions, it faces the problem of a high recombination rate of

* Corresponding author.
** Corresponding author.
E-mail addresses: cuijun@buct.edu.cn (J. Cui), jiang.yu@craes.org.cn (Y. Jiang).

https://doi.org/10.1016/j.ese.2025.100639

electron–hole pairs, which restricts catalytic efficiency [14,15]. On the other hand, only a single energy source is typically used, and its ability to handle complex environmental pollutants is insufficient [16]. Piezo-photocatalytic technology innovatively combines mechanical energy and solar energy to drive redox reactions [17], effectively overcoming the bottleneck of the high recombination rate of electron–hole pairs in traditional photocatalysis and significantly enhancing photocatalytic performance [13,18].

Molybdenum disulfide (MoS_2), a typical transition-metal dichalcogenide, offers significant promise for piezo- and photocatalysis due to its layered structure and tunable electronic properties [19,20]. However, pristine MoS_2 suffers from low catalytic efficiency and insufficient charge separation in practical applications, limiting its large-scale use [21]. To solve this problem, researchers have extensively studied defect engineering and element doping [22,23]. While sulfur vacancies (SVs) improve MoS_2's catalytic performance [19,23], they also reduce its carrier lifetime and structural stability [24–26].

In comparison, oxygen doping can not only repair SVs and enhance material stability but also optimize the piezoelectric response by changing the symmetry of the MoS_2 structure [27], providing a new direction for improving catalytic performance [28]. Research on low-concentration CBZ degradation via oxygen-doped MoS_2 in piezo-photocatalysis is preliminary; the links between the electronic structure, charge separation, and catalytic performance remain poorly understood. In addition, traditional heteroatom doping methods suffer from drawbacks such as complex preparation processes and uneven dopant distribution [29–31], which further hinder the in-depth exploration of the piezoelectric photocatalytic performance of oxygen-doped MoS_2 at the mechanistic level. It is worth emphasizing that the piezoelectric effect is highly significant in photocatalysis. When a piezoelectric material is subjected to pressure, it generates a piezoelectric potential. This potential can create a built-in electric field within the material, thereby promoting the separation of photogenerated carriers (electron–hole pairs) and reducing their recombination probability [17]. This process significantly improves the effective utilization of charges in photocatalytic reactions, thus enhancing catalytic efficiency.

To address prior challenges, we successfully synthesized O-MoS_2 using a simple, efficient hydrothermal method to replace some SVs in sulfur-deficient MoS_2 with oxygen. This study systematically investigated how CBZ degrades under combined piezoelectricity, photocatalysis, and piezo-photocatalysis. Through a combination of theoretical calculations and experimental verification, we conducted an in-depth analysis of the mechanism by which oxygen doping influences the electronic distribution, charge separation efficiency, and catalytic performance of MoS_2. The results of this study are expected to fill the gaps in the literature on the piezo-photocatalytic mechanism of oxygen-doped MoS_2 and lay a solid theoretical and practical foundation for the development of efficient and stable piezo-photocatalytic materials.

2. Materials and methods

2.1. Preparation of MoS_2 and O-MoS_2

The synthesis of MoS_2 and O-MoS_2 catalysts was carried out using a hydrothermal method. In a typical procedure, sodium molybdate dihydrate ($Na_2MoO_4{\cdot}2H_2O$, 1.2 g) and thiourea (CH_4N_2S, 0.66 g) were used as starting materials. The reagents were completely dissolved in 60 mL of a mixed ethanol/water solvent (7.6:52.4 v/v). The homogeneous solution was subsequently transferred into a 100 mL Teflon-lined stainless-steel reactor and maintained at 220 °C for 24 h. After the reaction, the resulting O_1-MoS_2 material was isolated through centrifugation, followed by sequential washing with ethanol–water mixtures. The purified product was then dried under a vacuum at 60 °C. Samples with different compositions of MoS_2 and O-MoS_2 were obtained by varying the molar ratios of the precursors, as detailed in the Supplementary Materials (Supplementary Table S1). Please refer to Supplementary Text S1 for a comprehensive list of all chemicals and electrode details.

2.2. Characterization of piezo-photocatalysts

The surface morphology of the samples was investigated by a scanning electron microscope (SEM; S-4800, Hitachi, Japan) equipped with an energy-dispersive spectrometer (EDS) and a high-resolution transmission electron microscope (HRTEM; JEM-2100, JEOL, Japan). Subsequently, the sample size distribution was analyzed using GMS 3 software. Crystal structure was characterized by X-ray diffraction (XRD) on an Ultima IV diffractometer (Rigaku, Japan) at a scanning rate of 2° min^{-1}. High-resolution X-ray photoelectron spectra (Mo 3 d, S 2p, O 1s, and C 1s) were acquired using an ESCALAB 250Xi spectrometer (Thermo Fisher Scientific, USA). Ultraviolet–visible diffuse reflectance spectra (UV–vis DRS) were collected using an Ultima IV spectrometer (Rigaku, Japan). Piezoelectric properties were evaluated using a piezoresponse force microscope (PFM) using a Dimension Icon atomic force microscope (Bruker, Germany), and the surface potential was detected using Kelvin probe force microscopy (KPFM). Molybdenum concentrations were measured using an inductively coupled plasma mass spectrometry using an instrument from Thermo Fisher Scientific (USA).

Working electrodes were prepared by ultrasonically blending 10 mg of catalyst powder, 50 μL of Nafion, and 5 mL of ethanol in a centrifuge tube. The homogeneous mixture was drop-cast onto indium tin oxide glass and followed by natural air-drying in a laboratory environment for 96 h. All piezo-photoelectrochemical tests, such as chronoamperometry (I–T), electrochemical impedance spectroscopy (EIS), cyclic voltammetry (CV), and Mott-Schottky tests, were carried out in a three-electrode system using a PGSTAT204 electrochemical workstation (Metrohm, Switzerland). For all electrochemical tests, 0.5 mol L^{-1} Na_2SO_4 was used as the electrolyte, except for CV measurements to determine the electrochemically active surface area (ECSA), where 0.5 mol L^{-1} H_2SO_4 was used. The sonication conditions were based on a BILON-1000Y ultrasonic unit (BILON, China).

2.3. Evaluation of degradation performance

To evaluate the catalytic performance, 0.01 g of each catalyst was added to 50 mL of a CBZ solution at 2 mg L^{-1}. Notably, this concentration is considered low in the field of photocatalytic mechanism research and is relatively close to the concentration of CBZ in the environment [12,32–37]. Subsequently, degradation experiments were conducted under four conditions: in the dark, under visible-light irradiation, with ultrasonic treatment, and under combined ultrasound and visible-light irradiation.

The separation between the light source and the bottom of the reaction container was set at 25 cm. This distance ensures that the reaction solution is fully covered by the light source while minimizing the thermal effect of the heat generated by the light source on the reaction solution through the appropriate spacing. Simulated sunlight was provided by a light source (HSX-F300, NBeT, China) equipped with a 350 nm filter. The light source intensity was 200–10000 mW cm^{-2}, and the light source wavelength ranged from 300 to 2500 nm. The ultrasound machine was provided by a Spring Rain ultrasonic cleaner (China).

The total organic carbon (TOC) values of the solutions obtained after reactions under different reaction conditions were measured using a TOC analyzer (TOC-L CPH, Shimadzu, Japan). CBZ concentrations were quantified by high-performance liquid chromatography (HPLC) using an HPLC system (Agilent, USA) equipped with a C18 column from Phenomenex (California, USA). An ultra-high-performance liquid chromatography tandem mass spectrometry device (Micromass Xevo TQD, Waters, USA) was used to pinpoint major intermediate products. Free radical generation was detected by an electron paramagnetic resonance (EPR) spectrometer with a Bruker Elexsys E560 system (USA). Active-species quenching experiments were conducted to identify the free radicals responsible for the degradation. Using factor analysis, the effects of pH, ultrasonic power, catalyst concentration, pollutant concentration, and pollutant type on the catalysts' degradation performance were analyzed. For specific experimental details, please refer to Supplementary Text S2.

2.4. Theoretical calculations and finite element simulation

We modeled the interactions using DFT with the Generalized Gradient Approximation–Perdew-Burke-Ernzerhof exchange-correlation functional. We applied an on-site Coulomb correction (where U–J, the difference between the Hubbard Coulomb interaction parameter (U) and the Hund's exchange parameter (J), is set to 5 eV)) to the d atomic orbital of molybdenum. The plane-wave cutoff energy was set at 259 eV. We employed the standard (blocked Davidson) algorithm with reciprocal-space projection operators and required electron convergence criterion to 1.0×10^{-5} eV. Based on the requirement for a k-point spacing of 0.5 $Å^{-1}$, a $1 \times 1 \times 1$ k-point grid was obtained. The actual k-point spacing was $0.46 \times 0.46 \times 0.28$ $Å^{-1}$, and we centered the grid at the gamma point. We used a Gaussian smearing with a width of 0.05 eV. Under the force-field condition, an additional external pressure of 1 GPa was applied to the aforementioned parameters.

A single-petal structure was constructed by simulating the O-MoS_2 edge curvature using the "image to curve" function in COMSOL Multiphysics 6.3, based on the single-petal structure [38,39]. We then rotated and assembled these petals to obtain a flower-like O-MoS_2 architecture. The connection point of the single petal was set to zero potential and constrained as a fixed value. To study the effect of internal forces on the piezoelectric strain response, we applied compressive stresses of 1 GPa and 2 GPa along the *z*-axis from the upper surface to the lower surface.

3. Results and discussion

3.1. Characterization of catalysts

In this study, $Na_2MoO_4{\cdot}2H_2O$ served as the molybdenum precursor, and ethanol was used as the oxygen source. A series of oxygen-doped MoS_2 materials (labeled $O_{(1-6)}$-MoS_2) were successfully synthesized using a hydrothermal method. Different oxygen doping levels in MoS_2 were precisely achieved by adjusting the amount of CH_4N_2S added (Fig. 1a, Supplementary Table S1). By adjusting the amount of CH_4N_2S added, the degree of oxygen substitution for SVs can be regulated, thereby achieving the control of different oxygen doping levels in MoS_2 (Fig. 1a–Supplementary Table S1).

The results of morphological and structural characterization, as shown in SEM images, reveal that all catalysts exhibit flake-like layered MoS_2 structures (Supplementary Fig. S1). Further analysis revealed that the particle size of the O-MoS_2 was positively correlated with sulfur content. The particle diameter gradually decreased from 2.4 ± 0.04 μm of MoS_2 to 1.6 ± 0.03 μm of O_6-MoS_2 (Supplementary Fig. S2 and Table S2). The EDS patterns confirmed that the elements Mo, S, and O were uniformly distributed in the O-MoS_2 samples (Supplementary Fig. S3–S9). The HRTEM images indicated that, compared to that of MoS_2, the structure of O-MoS_2 underwent distortion and featured an increase in active sites (Fig. 1b–d, Supplementary Fig. S10). Moreover, as sulfur content decreased, the O-MoS_2 structure showed a marked increase in disorder. According to crystal structure analysis, the XRD spectra revealed that all samples' diffraction peaks matched those of the hexagonal structure of MoS_2 (PDF#97-003-1067, corresponding to the 2H phase, a thermodynamically stable hexagonal layered crystal structure) (Fig. 1e). Oxygen doping resulted in significant broadening of the (002), (100), and (110) diffraction peaks, as well as shifting their distinct shifting to lower angles. Among these, the (002) peak exhibited the most prominent shift to lower angles [40]. In contrast, the diffraction peaks of (100) and (110) were not significantly affected by the decrease in sulfur content. This phenomenon was attributed to the incorporation of oxygen, which reduces the crystallinity of molybdenum disulfide and disrupts its inversion symmetry [7]. Meanwhile, the introduction of oxygen atoms increases electrostatic repulsion between layers, ultimately widening the interlayer spacing.

The surface electronic states and chemical composition of O-MoS_2 were comprehensively analyzed using X-ray photoelectron spectroscopy (XPS). The Mo 3 d peaks in all samples exhibited high similarity, showing comparable chemical states (Fig. 1f). Deconvolution analysis of the high-resolution Mo spectra identified the characteristic peaks of Mo–S bonds at $3d_{3/2}$ (232.7 eV) and $3d_{5/2}$ (229.4 eV), as well as the characteristic peaks of Mo–O bonds at $d_{3/2}$ (236.3 eV) and $3d_{5/2}$ (233.8 eV) [41]. The deconvolution analysis of the high-resolution S spectrum identified the characteristic peaks of S(II) at $2p_{1/2}$ (163.6 eV) and $2p_{3/2}$ (162.3 eV). The broad peak observed at 169.5 eV was attributed to SO_4^{2-} formed via the partial oxidation of certain sulfur species [42]. In addition, the XPS spectrum (Fig. 1g) showed lattice oxygen at 531.1 eV and adsorbed oxygen at 532.1 eV [43]. To further clarify the quantitative relationship between the oxygen doping level and defect repair, XPS area-integration analysis was performed. The XPS area-integration data indicated that a decrease in the amount of CH_4N_2S led to an increase in oxygen doping in O-MoS_2. Specifically, as the sulfur content decreased, the proportion of peak areas associated with Mo–O bonds and lattice oxygen gradually increased (Supplementary Table S3), which directly reflected the increase in the number of Mo–O bonds. Additionally, the shift of Mo 3 d and S 2p peaks to lower binding energies further confirmed the increase in oxygen content in O-MoS_2 [43]. These provided a quantitative correlation between oxygen doping and changes in chemical bonds, which were closely related to SV repair.

In addition, based on XPS atomic percentages, the O-MoS_2 models were constructed using the DFT (Supplementary Table S4) [44,45]. By calculating the activation energy (E_a) of oxygen atoms at different positions within the structure, we found that the oxygen atoms in SVs had much lower activation energy than those at S-atom sites or positioned randomly in the lattice (Supplementary Fig. S11). This indicates that the introduced oxygen atoms preferentially occupied the preexisting SV sites and provides a quantitative basis for the defect-repair process from an energy perspective. The results of the DFT energy calculation showed that, compared with undoped MoS_2, O-MoS_2 had a more stable state, which further explained the effect of oxygen doping from the perspective of the relationship between energy and defect repair (Supplementary Fig. S12). In conclusion, these findings strongly support the successful incorporation of oxygen atoms into MoS_2 and clarify the relationship between oxygen doping level and defect repair.

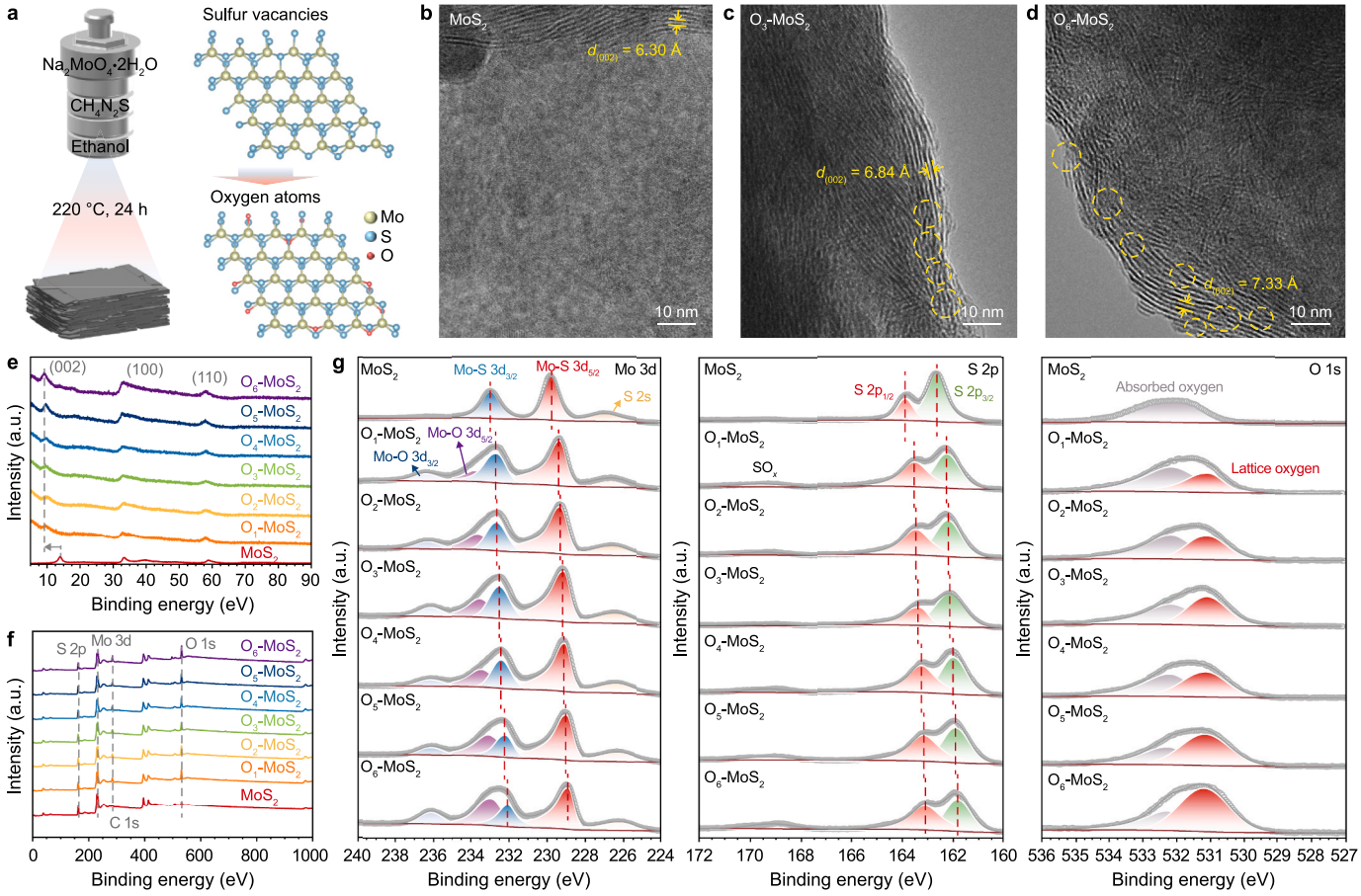

Fig. 1. Characterization of O-MoS_2: Synthesis, morphology, and electronic structure. **a**, Schematic of preparation of O-MoS_2. **b**–**d**, High-resolution transmission electron microscope diagram of MoS_2 (**b**), O_3-MoS_2 (**c**), and O_6-MoS_2 (**d**). The yellow dashed lines indicate the positions where lattice distortion occurs. **e**, X-ray diffraction patterns. **f**, X-ray photoelectron spectroscopy (XPS) survey spectra. **g**, High-resolution XPS spectra of Mo 3 d, S 2p, and O 1s.

The band structure plays a pivotal role in determining the piezoelectric-photocatalytic performance because it directly governs charge separation efficiency, carrier migration behavior, and the generation capability of active species [46]. The optical absorption properties and band structure of the samples were systematically characterized using UV–vis DRS and valence-band X-ray photoelectron spectroscopy (VB-XPS). Compared to MoS_2, O-MoS_2 demonstrated a substantially extended optical absorption range, indicating that oxygen doping not only preserved the material's ultraviolet absorption capability but also expanded its absorption into the visible light region (Fig. 2a). By applying the Kubelka–Munk equation (Supplementary Text S3 equation (1) [46]), the band gaps (E_g) of the different samples were determined to be 2.30 eV (MoS_2), 2.29 eV (O_1-MoS_2), 2.24 eV (O_2-MoS_2), 2.18 eV (O_3-MoS_2), 2.10 eV (O_4-MoS_2), 2.05 eV (O_5-MoS_2), and 1.94 eV (O_6-MoS_2) (Fig. 2b, Supplementary Fig. S13). The lower E_g, caused by oxygen doping and the resulting defect states, allowed more electron transitions, leading to significantly improved light absorption. Based on the VB-XPS results and Supplementary Text S3 equation (2) [37], a schematic of the band structure of O-MoS_2 was constructed (Fig. 2c) [36,47]. O-MoS_2 has the potential to generate superoxide radicals ($\bullet O_2^-$) and singlet oxygen ($^1O_2$). These active species could further promote the generation of reactive species during the photocatalytic degradation process. According to the partial density of states (PDOS) analysis, the conduction band (E_{CB}) and valence band (E_{VB}) were predominantly dominated by S 3p and Mo 4 d orbitals (Fig. 2d and e, Supplementary Fig. S14).

Oxygen doping resulted in a notable negative shift in the E_{VB}, thereby significantly enhancing light absorption and carrier separation efficiency. Notably, as the proportion of oxygen doping gradually increased, the proportion of O 2p orbitals in the entire system also gradually increased (Supplementary Table S5). This change in oxygen doping significantly affected the material's electronic structure, as evidenced by a distinct negative shift in the valence band. This negative shift effectively enhanced the material's light-absorption capacity and significantly improved the separation efficiency of photogenerated carriers (N_d) (Fig. 2f–Supplementary Table S6 and Text S3 equation (3) [48]) [49], further optimizing the photocatalytic performance of MoS_2.

3.2. Piezo-photocatalytic degradation performance

To explore the relationship between photocatalysis and piezocatalysis in O-MoS_2, the catalytic performance of O-MoS_2 in the degradation of CBZ was analyzed. Experiments were conducted under four conditions: dark, visible light, ultrasound, and a combination of ultrasound and visible light (Fig. 3a–c, Supplementary Fig. S15). In the dark, all samples reached adsorption equilibrium within 90 min, achieving a maximum adsorption rate of 14.2%. Oxygen doping had no significant effect on the adsorption performance of MoS_2 in the dark. Under visible light irradiation, the optimal O-MoS_2 (O_5-MoS_2) showed a 24.8% improvement in removal efficiency and a 2.8-fold increase in reaction rate constant (k_{obs}) compared to MoS_2 (Fig. 3d) [50]. Notably, the photocatalytic

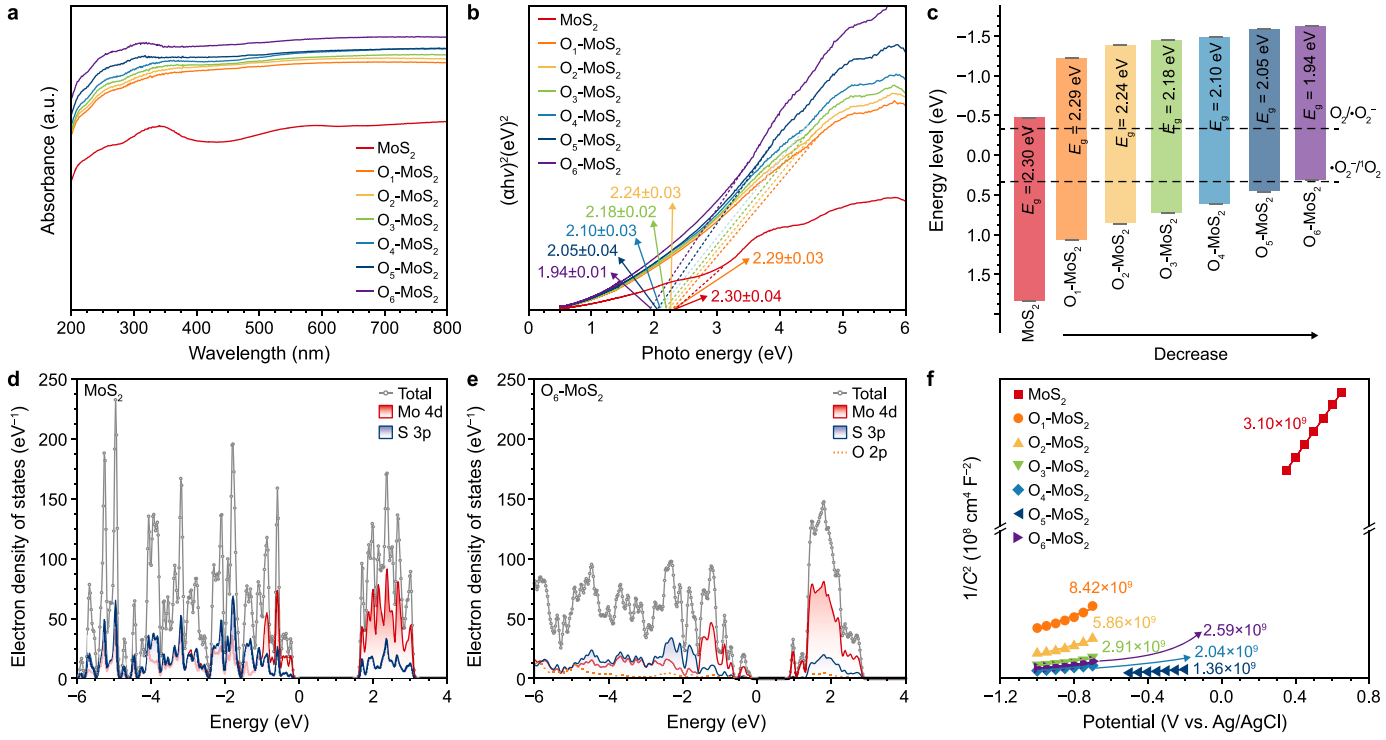

Fig. 2. Optoelectronic and band Structure characterization of MoS_2 and O-MoS_2. **a**, Ultraviolet–visible diffuse reflectance spectra. **b**, Valence band X-ray photoelectron spectroscopy spectra. Numbers indicate the intersections of the dashed line with the *x*-axis, corresponding to the free-radical formation potential. **c**, Energy band diagram. E_g: band gap. **d**, The density of states of MoS_2. **e**, The density of states of O_6-MoS_2. **f**, Mott–Schottky plots. The numbers in the figure represent the slope of the tangent to the Mott–Schottky curves.

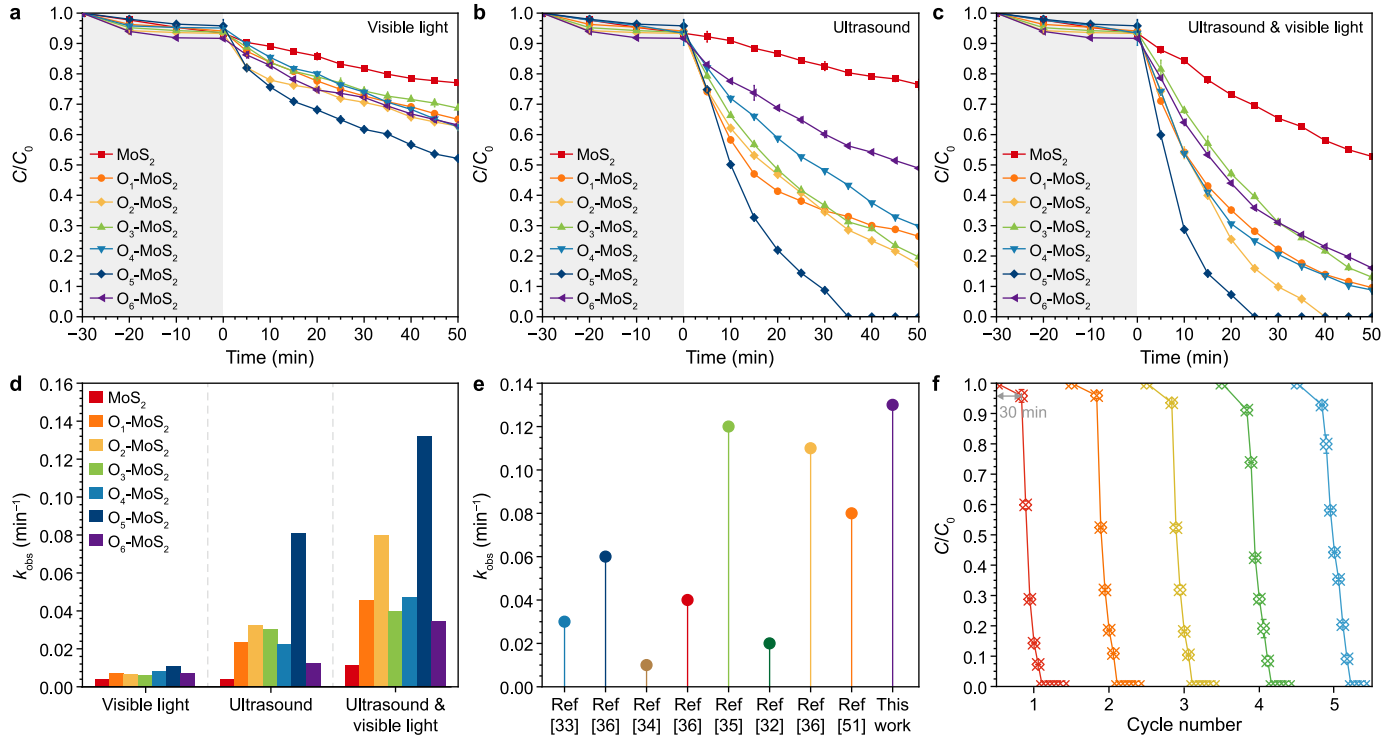

Fig. 3. Evaluating the efficiency and sustainability of carbamazepine (CBZ) degradation systems. **a**–**c**, Degradation performance under different conditions: visible light (**a**), 480 W ultrasound (**b**), and visible light and 480 W ultrasound (**c**). **d**, Comparison of reaction rate constants in different systems. **e**, Rate constants for CBZ degradation in the literature and the rate constant in this study. **f**, Stability and reusability tests. The first 30 min (panel **f**; shaded gray regions in panels **a**–**c**) correspond to the dark adsorption stage.

performance of O_6-MoS_2 was comparable to that of catalysts with low and medium oxygen content, suggesting that excessive oxygen doping may introduce defects that inhibit photocatalytic activity.

Under ultrasonic conditions, O-MoS_2 catalysts exhibited enhanced piezocatalytic activity compared to undoped MoS_2 (Fig. 3b). The CBZ removal rate increased from 23.6% (MoS_2) to 100% (O_5-MoS_2), and k_{obs} increased from 4.2×10^{-3} min^{-1} (MoS_2) to 80.8×10^{-3} min^{-1} (O_5-MoS_2). Among them, O_5-MoS_2 displayed the highest piezocatalytic activity, followed by O_2-MoS_2, indicating that the piezocatalytic activity initially increased, then decreased, and subsequently increased again with increasing oxygen content. Moreover, O_1-MoS_2, O_3-MoS_2, and O_4-MoS_2 exhibited similar piezo-catalytic degradation, with O_6-MoS_2 showing minimal piezoelectric enhancement. This indicates that, before the oxygen-doping amount reaches a certain level, piezocatalytic activity increases substantially. However, once this optimal doping amount is reached, further increases in piezocatalytic activity may be limited by lattice disorder, leading to a decrease.

Notably, the influence of oxygen-doping content on the performance of O-MoS_2 in synergistic catalysis by visible light and ultrasound followed a trend similar to that observed for its impact on pure ultrasonic catalysis. Moreover, under the synergistic effects of visible light and ultrasound, the removal efficiency of CBZ by all materials was significantly higher than that in the individual photocatalytic or piezocatalytic processes (Fig. 3c). Ultrasound significantly enhanced the photocatalytic activity of O-MoS_2. MoS_2 achieved a CBZ removal rate of 47.2% within 50 min, while O_5-MoS_2 and O_4-MoS_2 achieved 100% CBZ removal within 25 min and 40 min, respectively. During the piezo-photocatalytic degradation process, the k_{obs} of various catalysts showed the following order: O_5-MoS_2 (0.13 min^{-1}) > O_2-MoS_2 (0.08 min^{-1}) > O_4-MoS_2 = O_1-MoS_2 (0.05 min^{-1}) > O_3-MoS_2 = O_6-MoS_2 (0.04 min^{-1}). Notably, the k_{obs} value of O_5-MoS_2 exceeded the relevant values reported in most of the literature (Supplementary Table S7) [32–36,51]. This confirmed the superior piezoelectric-photocatalytic performance of O-MoS_2 (Fig. 3e). Meanwhile, the TOC mineralization rate of O_5-MoS_2 under the synergistic condition reached 68.8%, which was 3 times and 1.7 times that of individual photocatalysis and individual ultrasonic degradation (Supplementary Fig. S16), respectively, indicating that the synergistic system could achieve efficient mineralization.

Stability tests showed that after five degradation cycles, O_5-MoS_2 could still achieve complete removal of CBZ within 35 min under the synergistic effect of ultrasound and visible light (Fig. 3f). There was no obvious change in the morphology of the material before and after degradation (Supplementary Fig. S17). The XRD patterns (Supplementary Fig. S18) and XPS spectra (Supplementary Fig. S19) remained consistent, confirming its good stability. In addition, the material exhibited excellent pH adaptability and maintained efficient degradation performance even under low ultrasonic power (Supplementary Fig. S20). Under catalyst dosage of 0.1–0.3 mg L^{-1} and pollutant concentration of 1–3 mg L^{-1}, the synergistic system achieved 100% degradation of CBZ within 40 min. Extended experiments showed that O_5-MoS also exhibited good degradation of sulfamethazine, tetracycline, and methylene blue. In the actual surface water system, CBZ degradation could be completed within 35 min under the synergistic condition. The above results confirm that O_5-MoS_2 has good practical application potential.

3.3. Degradation pathway analysis

Two reactive oxygen species ($\bullet O_2^-$ and $^1O_2$) were identified as contributors to the degradation of CBZ through EPR tests (Supplementary Fig. S21). The signals from these active species were significantly enhanced when ultrasound was added to the photocatalytic system. This finding indicates that the ultrasound-induced cavitation effect and mechanical vibration effectively enhanced the separation of photogenerated electron–hole pairs and improved the generation efficiency of the active species. In addition, through radical quenching experiments, there was no •OH in the system and $\bullet O_2^-$ was the main reactive species (56.7%), followed by $^1O_2$ (25.8%) and h^+ (19.2%) (Supplementary Fig. S22).

The intermediate products generated during CBZ degradation were analyzed using a Waters UHPLC-MS system. Sixteen intermediate products were identified (Supplementary Table S8), and two primary degradation pathways for CBZ during the piezo-photocatalytic process were proposed (Fig. 4a) [9,32–34,52,53]. In Pathway I, oxidative ring contraction was identified as the dominant mechanism. CBZ was initially converted to the common intermediate P1. Subsequently, under the influence of reactive species, P1 underwent cleavage and recombination, further generating P2, P5, and P9. In Pathway II, P10 was oxidized from CBZ or P9; additionally, ring cleavage of P7 yielded P11. As the reaction progressed, the intermediate products underwent further deamination and dehydrogenation reactions, ultimately converting large molecules into smaller ones and completing the mineralization process.

The toxicity of CBZ's degradation products was determined using the model of Ecological Structure Activity Relationships (ECOSAR) to understand changes in toxicity during CBZ degradation. As shown in Fig. 4b–d (Supplementary Table S9), the toxicity of the degradation products decreased gradually as the reaction progressed. The results indicate that the piezo-photocatalytic process effectively degraded CBZ and significantly reduced its environmental impact. The molybdenum leaching rate was only about 1.9%. This low leaching level further confirms that the material is unlikely to cause secondary pollution during application and possesses favorable environmental safety and friendliness.

3.4. Analysis and discussion of the mechanism

To further elucidate the effect of oxygen doping level on the piezoelectric photocatalytic mechanism of O-MoS_2, a comprehensive series of photoelectrochemical experiments was conducted to evaluate its photoelectric conversion efficiency. EIS was used to investigate the photogenerated charge transfer behavior at the piezo-photocatalyst/electrolyte interface. In the dark, the charge-transfer resistance (R_{ct}) of all samples decreased (Fig. 5a, Supplementary Fig. S23 and Table S10). Oxygen doping effectively promoted charge–transfer kinetics in MoS_2 nanostructures [19]. Under visible-light irradiation, low- and medium-level oxygen doping decreased the R_{ct} of MoS_2, with O_5-MoS_2 reaching a minimum of 6.6 Ω. However, R_{ct} increased to 8.2 Ω in O_6-MoS_2 due to excessive oxygen doping, which disrupted the active sites and reduced their effectiveness. These findings were confirmed by ECSA measurements conducted under both dark and visible light conditions (Supplementary Fig. S24–S26). Moreover, the transient photocurrent (J_{photo}), piezoelectric photocurrent (J_{piezo}), and piezo-photocatalytic synergistic photocurrent responses ($J_{piezo\text{-}photo}$) of MoS_2 and O-MoS_2 were systematically evaluated to clarify the differences in charge separation efficiency during various catalytic processes [54]. The stabilized J_{photo} values of all samples were relatively similar, with O_5-MoS_2 showing only a 0.33 μA cm^{-2} increase compared to MoS_2 (Fig. 5b). The photocurrent density retention efficiency (*PDRE*) was 60.8% for MoS_2 and 100% for O_5-MoS_2 (Supplementary Text S3 equation (4) [46]). These results indicate that the oxygen-doping proportion had limited effects on light performance but significantly improved the photostability of MoS_2. Under ultrasonic conditions, all materials exhibited

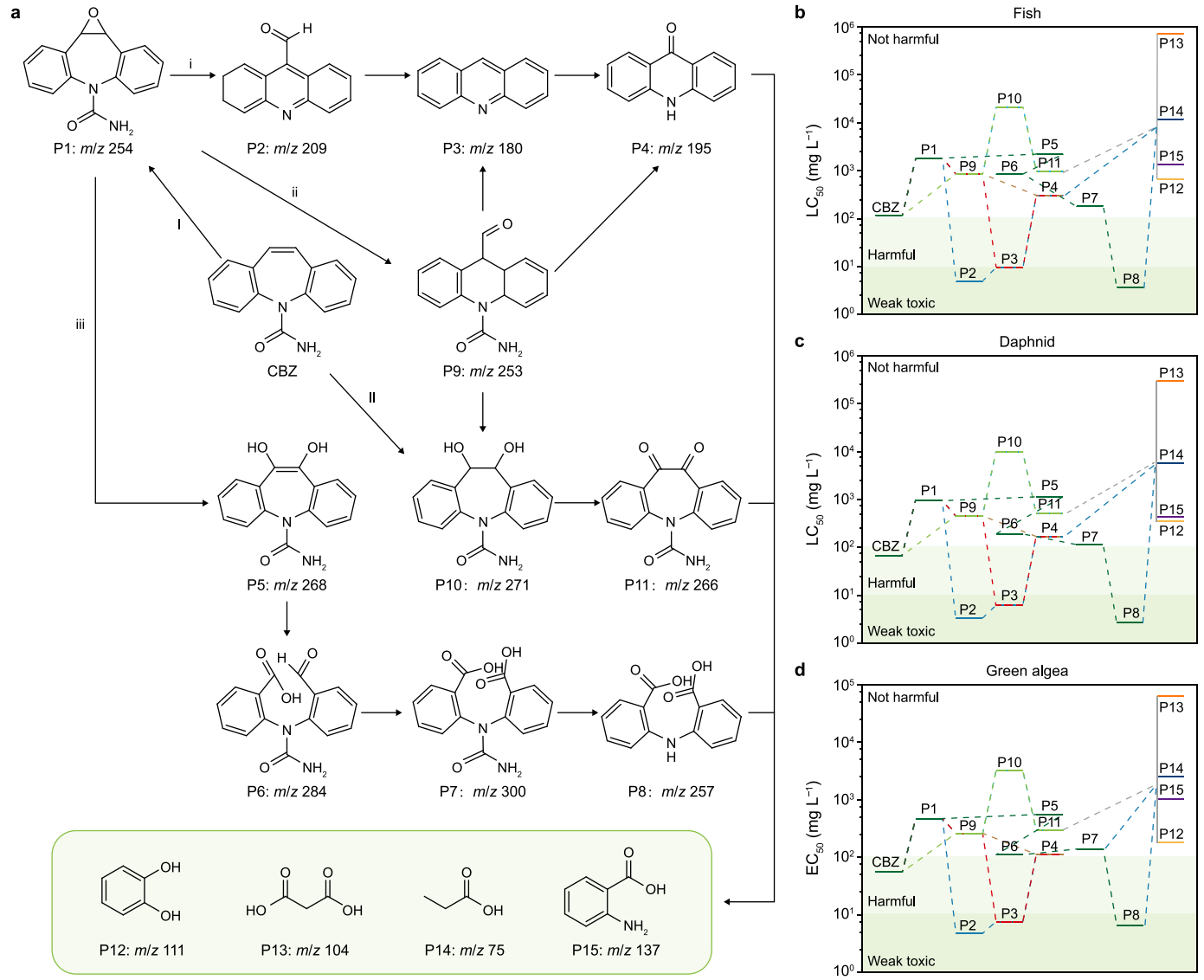

Fig. 4. Carbamazepine (CBZ) degradation pathways and ecotoxicity evaluation across multiple organisms. **a**, Possible degradation pathways of CBZ. Roman numerals I and II denote the primary degradation pathways, while lowercase roman numerals i–ii represent the secondary degradation pathways. Degradation products are denoted as PX ($X = 1, 2, 3, \ldots$). **b**–**d**, environmental toxicity assessment of degradation products: fish (**b**), daphnid (**c**), and green algae (**d**). Strong toxic: Half-lethal concentration/Half-effect concentration (LC_{50}/EC_{50}) < 1 mg L^{-1}, weak toxic: 1 mg L^{-1} < LC_{50}/EC_{50} < 10 mg L^{-1}, harmful: 10 mg L^{-1} < LC_{50}/EC_{50} < 100 mg L^{-1}, not harmful: LC_{50}/EC_{50} > 100 mg L^{-1}.

excellent instantaneous-response capabilities, reflecting their superior piezoelectric sensitivity. Compared to MoS_2, the J_{piezo} of O-MoS_2 was significantly enhanced. Under the synergistic action of ultrasound and visible light, the $J_{piezo\text{-}photo}$ was further increased, surpassing both the individual piezoelectric (J_{piezo}) and photocurrent (J_{photo}) values (Fig. 5c, Supplementary Fig. S27). In descending order of $J_{piezo\text{-}photo}$ values, they were O_5-MoS_2 (4.18 μA cm^{-2}) > O_2-MoS_2 (4.12 μA cm^{-2}) > O_3-MoS_2 (3.53 μA cm^{-2}) > O_4-MoS_2 (3 μA cm^{-2}) > O_6-MoS_2 (2.53 μA cm^{-2}) > O_1-MoS_2 (1.78 μA cm^{-2}) > MoS_2 (0.85 μA cm^{-2}). Moderate and high proportions of oxygen doping significantly enhanced catalytic performance under ultrasonic conditions. However, when the proportion of oxygen doping was too high, the activity of O-MoS_2 decreased instead. These observations confirm the degradation performance discussed previously. Meanwhile, J_{piezo} and $J_{piezo\text{-}photo}$ values showed a strong linear relationship with ultrasonic power across different ultrasonic power conditions (Supplementary Fig. S28). This indicates that ultrasound significantly enhanced the charge-separation efficiency and carrier mobility in photocatalysis.

The piezoelectric property of the material originates from its noncentrosymmetric crystal structure and excellent deformation ability under external force [55]. To thoroughly analyze this property, this research calculated the Bader charges, bond lengths, and bond angles of MoS_2 and O-MoS_2 at atmospheric pressure and 1 GPa pressure based on DFT [56]. The Bader charge value of the Mo–O bond (2.08–2.36 e^-) was found to be significantly higher than that of the Mo–S bond (1.59–1.94 e^-) (Fig. 5d, Supplementary Fig. S29–S33 and Table S11), suggesting Mo–O's higher reactivity. Meanwhile, both the Mo–S and Mo–O bonds showed clear stretching. The stretching amplitude of the Mo–S bond was significantly greater than that of the Mo–O bond (Supplementary Table S12). Under pressure, the bond-angle parameters also changed accordingly (Supplementary Table S13). The above results indicate that O-MoS_2 exhibited excellent structural deformation ability and polarization characteristics under external force,

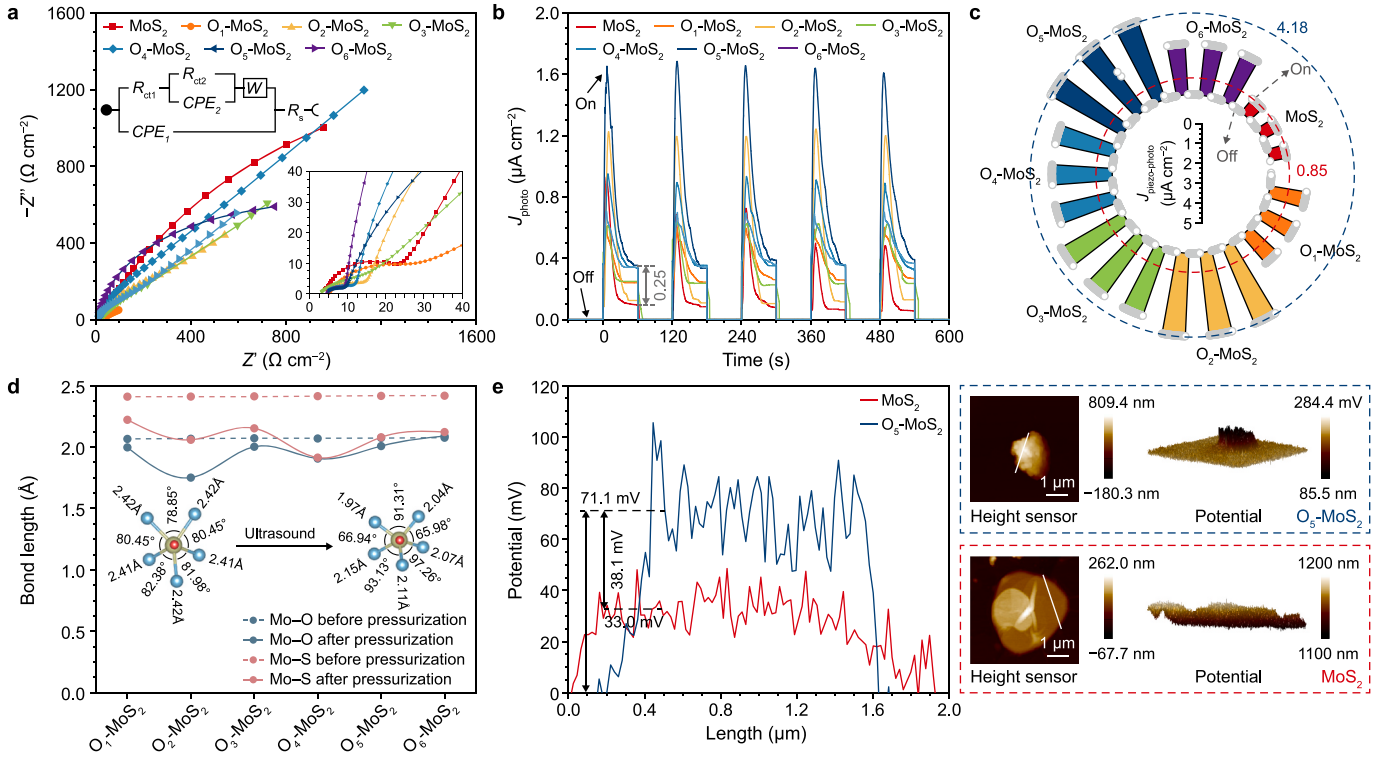

Fig. 5. Electrochemical response and structural alterations of MoS_2 and O-MoS_2 under visible light, ultrasound, and pressure. **a**, Electrochemical impedance spectroscopy (EIS) curves under visible light irradiation. The inset is an enlarged view of the EIS curves. **b**, Transient current density-time curves under on-off cycles of visible light. The stable J_{photo} difference between MoS_2 and O_5-MoS_2 is 0.25 μA cm^{-2} **c**, Transient current density–time curves under on–off cycles of visible light and 480 W ultrasound. **d**, The charge values of Mo, S, and O under ambient pressure and 1 GPa pressure. The inset figure is the schematic diagram of Mo–O and Mo–S bond lengths and S–Mo–S bond angles. **e**, Surface potential curves. The numbers marked in the left panel represent the average potential values. The right panels are topographic images and Kelvin probe force microscopy potential images for MoS_2 and O_5-MoS_2.

thereby providing a theoretical basis at the structural level for its enhanced piezoelectric performance. Further analysis revealed that mechanical deformation induced by an external force redistributed the Bader charges of Mo, S, and O atoms in O-MoS_2, thereby forming an internal electric field, thereby revealing the essential mechanism of its piezoelectric effect. COMSOL Multiphysics was used to evaluate deformation-induced piezoelectric activity. The O-MoS_2 model was constructed based on the morphology observed in SEM images and the physicochemical parameters of MoS_2. Under stimuli of 1 GPa and 2 GPa, substantial deformation and potential intensity were observed (Supplementary Fig. S34) [38,39]. These results indicate that O-MoS_2 nanosheets exhibit robust piezoelectric activity.

To evaluate the enhancement effect of piezoelectric properties on charge separation efficiency, this study systematically characterized parameters related to the piezoelectric field. In PFM measurements, both MoS_2 and O_5-MoS_2 demonstrated typical butterfly-shaped amplitude loops and hysteresis curves under an applied voltage of ±10 V (Supplementary Fig. S35), further confirming their piezoelectric characteristics [57,58]. Additionally, the d_{33} value of O_5-MoS_2 (63 p.m. V^{-1}) was substantially higher than that of MoS_2 (26 p.m. V^{-1}) (Supplementary Fig. S36), highlighting the superior piezoelectric performance of O_5-MoS_2. KPFM measurements provided a clear visualization of the surface potential distribution. The results indicate that the surface potential of O_5-MoS_2 exceeded that of MoS_2 by 38.1 mV (Fig. 5e), reflecting a stronger built-in electric field in O_5-MoS_2. This enhanced electric field provided a stronger driving force for accelerating charge-carrier separation [58]. The built-in potential, which drives the directional migration of photogenerated charges, was significantly enhanced under ultrasonic-visible light conditions for both MoS_2 and O-MoS_2. Notably, O_5-MoS_2 (0.19 V) exhibited a higher built-in potential intensity than MoS_2 (0.13 V) (Supplementary Fig. S37). Further research revealed that the magnitude order of the built-in potential of O-MoS_2 with different oxygen doping amounts was extremely similar to the distribution of $J_{piezo\text{-}photo}$ mentioned earlier, suggesting that oxygen doping effectively enhanced the charge driving force in O-MoS_2.

Together, these results support the following piezo-photocatalytic mechanism of O-MoS_2 (Fig. 6). The Fermi level of O-MoS_2 was lower than that of the CBZ solution (Supplementary Table S14), which led to the formation of a positive band-bending structure in the space-charge region on the catalyst surface [59]. Under visible-light irradiation, O-MoS_2 absorbed photon energy to generate electron–hole pairs, which tend to recombine easily without external assistance. After the introduction of ultrasound, due to O-MoS_2's oncentrosymmetric crystal structure, mechanical vibration caused the positive and negative charge centers to shift, generating an internal electric field that further bent the band downward. This not only lowered the energy barrier but also caused electrons and holes to move in opposite directions, reducing recombination and improving utilization efficiency. The separated electrons reacted with adsorbed O_2 to produce $\bullet O_2^-$, and h^+ generated $^1O_2$, which promoted the degradation of CBZ. The synergy between piezoelectricity and light stems from the energy provided by light that generates charge carriers and the improved charge separation resulting from the internal electric field induced by ultrasound through the piezoelectric effect, which greatly improves interfacial charge-separation efficiency, intensifies the photocatalytic process, enables more holes and electrons to

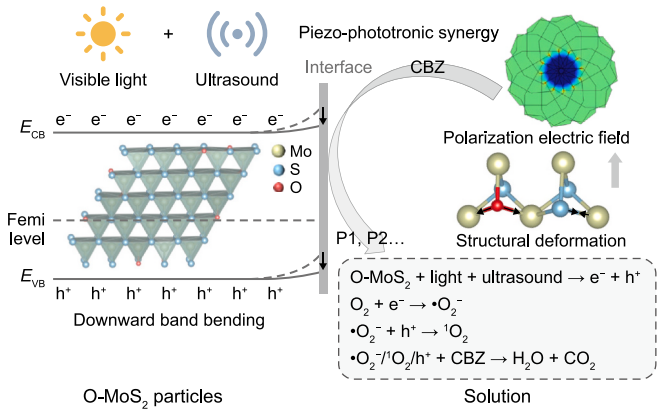

Fig. 6. Schematic illustration of piezoelectrically enhanced photocatalysis of O-MoS_2. CBZ: carbamazepine. Degradation products are denoted as PX (X = 1, 2, 3, …). E_{CB}: the conduction band. E_{VB}: the valence band.

participate in the reaction, and significantly enhances the piezo-photocatalytic degradation performance. In addition, the Mo–S bond was a reactive chemical bond. Under visible-light irradiation, as the proportion of oxygen doping in O-MoS_2 gradually increased, the number of reactive bonds increased. Meanwhile, the band gap of O-MoS_2 decreased gradually, and its photoactivity increased accordingly. However, when the oxygen-doping proportion exceeded a specific threshold, the degree of lattice disorder increased significantly, negatively affecting photocatalytic activity. Compared with the performance under pure photocatalytic conditions, the proportion of oxygen doping had a more significant impact on ultrasonic catalytic performance. The driving force of the built-in potential enhanced the current density and the separation efficiency of electron–hole pairs, resulting in a variation trend of the piezoelectric catalytic performance of O-MoS_2 with the increase of oxygen doping ratio: first increasing, then decreasing, rising again to reach a maximum, and finally decreasing. Moreover, the impact of the oxygen-doping proportion on the synergistic catalytic effect was similar to that on the ultrasonic catalytic performance.

4. Conclusions

In this study, the piezo-photocatalytic performance of MoS_2 was successfully optimized via an oxygen-doping strategy. Oxygen doping at low, medium, and high levels enhanced the charge-separation efficiency and carrier concentration of MoS_2. DFT calculations, photoelectrochemical experiments, and COMSOL Multiphysics simulations indicated that oxygen doping at these levels increased the charge difference between Mo and S (from 1.77 e to 1.86 e), thereby enhancing catalytic activity. Under piezoelectric conditions, O-MoS_2 with high-level oxygen doping demonstrated excellent deformation ability and polarization characteristics under external force, along with an increase in the built-in potential (from 0.12 V to 0.19 V). This significantly improved the piezoelectric response and charge-separation efficiency of MoS_2. O_5-MoS_2 completed the degradation of CBZ within 25 min, and its k_{obs} was 11.4 times that of unmodified MoS_2. This study provides new insights into the impact of oxygen doping on the catalytic performance of MoS_2, and provides a theoretical basis and practical guidance for designing highly efficient, stable piezo-photocatalytic materials.

CRediT authorship contribution statement

Yanjiao Li: Writing - Original Draft, Visualization, Investigation, Formal Analysis, Data Curation, Conceptualization. **Lianfeng Wang:** Writing - Review & Editing, Methodology, Conceptualization. **Yuting Ning:** Writing - Review & Editing, Visualization, Formal Analysis. **Ying Yuan:** Resources, Conceptualization. **Xinping Fu:** Visualization, Formal analysis. **Jun Cui:** Writing - Review & Editing, Resources, Methodology, Conceptualization. **Yu Jiang:** Writing - Review & Editing, Resources, Investigation, Conceptualization.

Declaration of interest statement

The authors declare that they have no known competing financial interests or personal relationships that could have appeared to influence the work reported in this paper.

The author is an Editorial Board Member/Editor-in-Chief/Associate Editor/Guest Editor for this journal and was not involved in the editorial review or the decision to publish this article.

The authors declare the following financial interests/personal relationships which may be considered as potential competing interests:

Acknowledgements

This work was supported by the National Natural Science Foundation of China (Grant No. 52270055) and the Fundamental Research Funds for the Central Universities (Grant No. BUCTRC202209).

Appendix A. Supplementary data

Supplementary data to this article can be found online at https://doi.org/10.1016/j.ese.2025.100639.

References

[1] S. Zhang, J. Yang, H. Wang, S. Zhang, Enhanced photo Fenton-like AOP by N-doped and Cu–Fe loaded biochar for efficient sulfamethoxazole removal: economic synthesis, catalytic, performance and mechanism, Chemosphere 385 (2025) 144543, https://doi.org/10.1016/j.chemosphere.2025.144543.
[2] J. Xu, L. Wang, X. Mao, H. Zou, G. Liu, Enhanced electrochlorination for efficient ammonia oxidation facilitated by accelerating electron cycling on Co^{2+}/Co^{3+}, J. Environ. Chem. Eng. 13 (2025) 115415 https://doi.org/10.1016/j.jece.2025.115415.
[3] Y. Yang, X.-M. Zhao, R.W.S. Lai, Y. Liu, S. Liu, X. Jin, G.-J. Zhou, Decoding adverse effects of organic contaminants in the aquatic environment: a meta-analysis of species sensitivity, hazard prediction, and ecological risk assessment, Environ. Sci. Technol. 58 (2024) 18122–18132, https://doi.org/10.1021/acs.est.4c04862.
[4] D. Liu, C. Zhang, N. Yan, Y. Yan, H. Duan, Eutrophication exacerbated organic pollution in lakes across China during the 1980s–2010s, Water Res. 268 (2025) 122782, https://doi.org/10.1016/j.watres.2024.122782.
[5] L. Qiang, J. Cheng, J. Yi, J.M. Rotchell, X. Zhu, J. Zhou, Environmental concentration of carbamazepine accelerates fish embryonic development and disturbs larvae behavior, Ecotoxicology 25 (2016) 1426–1437, https://doi.org/10.1007/s10646-016-1694-y.
[6] Y. Kim, K. Choi, J. Jung, S. Park, P.-G. Kim, J. Park, Aquatic toxicity of acetaminophen, carbamazepine, cimetidine, diltiazem and six major sulfonamides, and their potential ecological risks in Korea, Environ. Int. 33 (2007) 370–375, https://doi.org/10.1016/j.envint.2006.11.017.
[7] W. Song, H. Fang, Z. Lei, R. Wang, C. Fu, F. Wang, Y. Fang, X. Du, Z. Wang, Z. Zhao, Insight into homogeneous activation of sodium hypochlorite by dithionite coupled with dissolved oxygen (DO@NaClO/DTN) for carbamazepine degradation, Water Res. 277 (2025) 123312, https://doi.org/10.1016/j.watres.2025.123312.
[8] D.B. Miklos, C. Remy, M. Jekel, K.G. Linden, J.E. Drewes, U. Hübner, Evaluation of advanced oxidation processes for water and wastewater treatment-A critical review, Water Res. 139 (2018) 118–131, https://doi.org/10.1016/j.watres.2018.03.042.
[9] C. Feng, Q. Gu, J. Rong, X. Zheng, Y. Zhang, Q. Liang, Z. Li, S. Xu, A twin S-

scheme $CoFe_2O_4$/VCNDA/$BiVO_4$ nanozyme for photo-auto-enzyme-coupled catalytic degradation of carbamazepine, Chem. Eng. J. 495 (2024) 153606, https://doi.org/10.1016/j.cej.2024.153606.
[10] X. Zhang, M. Kamali, X. Yu, M.E.V. Costa, L. Appels, D. Cabooter, R. Dewil, Kinetics and mechanisms of the carbamazepine degradation in aqueous media using novel iodate-assisted photochemical and photocatalytic systems, Sci. Total Environ. 825 (2022) 153871, https://doi.org/10.1016/j.scitotenv.2022.153871.
[11] Q. Liu, Z. Li, J. Li, F. Zhan, D. Zhai, Q. Sun, Z. Xiao, H. Luo, D. Zhang, Three dimensional $BaTiO_3$ piezoelectric ceramics coated with TiO_2 nanoarray for high performance of piezo-photoelectric catalysis, Nano Energy 98 (2022) 107267, https://doi.org/10.1016/j.nanoen.2022.107267.
[12] S. Wang, Y. Li, K. Lin, Z. Li, L. Xu, Z. Yin, J. Qiu, Z.w. Yang, Z. Song, Enhancing the piezoelectric properties and carrier separation efficiency to improves Bi_2NdO_4Cl piezo-photocatalytic performance by Ce ion doping, Appl. Surf. Sci. 694 (2025) 162841, https://doi.org/10.1016/j.apsusc.2025.162841.
[13] J. Lin, J. Du, Y. Zhu, Z. Chen, M. Wang, J. Zeng, Z. Li, D. Li, D. Gao, D. Wang, Enhanced piezoelectric photocatalytic activity of MXene/ZnS/Fe_3O_4 via three-in-one strategy based on dual Schottky heterojunction, interface electric field, and oxygen vacancy for pollutant degradation and removal, Water Res. 273 (2025) 123040, https://doi.org/10.1016/j.watres.2024.123040.
[14] H. Lei, M. Wu, F. Mo, S. Ji, X. Dong, Y. Jia, F. Wang, Z. Wu, Efficiently harvesting the ultrasonic vibration energy of two-dimensional graphitic carbon nitride for piezocatalytic degradation of dichlorophenols, Environ. Sci. Nano 8 (2021) 1398–1407, https://doi.org/10.1039/D0EN01028F.
[15] S. Yan, S. Sun, Z. Chen, X. Wang, Improved photocatalytic activity of $SrBi_2Nb_2O_9$ for the degradation of ciprofloxacin hydrochloride via piezoelectric-enhanced charge transfer, Chin. J. Struct. Chem. (2025) 100569, https://doi.org/10.1016/j.cjsc.2025.100569.
[16] Y. Liu, J. Li, B. Zhou, J. Bai, Q. Zheng, J. Zhang, W. Cai, Comparison of photoelectrochemical properties of TiO_2-nanotube-array photoanode prepared by anodization in different electrolyte, Environ. Chem. Lett. 7 (2009) 363–368, https://doi.org/10.1007/s10311-008-0180-z.
[17] H.-J. Jiang, Y.-L. Mei, W.-M. Liu, Z.-J. Wu, Enhanced piezo-photocatalytic activity of oxygen-deficient ZnO nanoparticles prepared by facile precipitation, Appl. Surf. Sci. 708 (2025) 163770, https://doi.org/10.1016/j.apsusc.2025.163770.
[18] Z. Li, P. Su, A. Wang, W. Su, J. Pu, F. Chen, Z. Ke, X. Luo, C. Li, Y. Wu, Sequential anaerobic-aerobic photocatalytic degradation of halogenated organic pollutants via dual-site confined carbon nitride, J. Hazard. Mater. 490 (2025) 137861, https://doi.org/10.1016/j.jhazmat.2025.137861.
[19] X. Chen, H. Xu, C. Liu, Z. Wang, R. Wang, J. Wang, R. Pan, J. Qi, Y. Wang, F. Meng, Synthesis and characterization of Vs-B/MoS_2 with double defects for efficient piezocatalytic antibiotic degradation and bacterial disinfection, Chem. Eng. J. 498 (2024) 155591, https://doi.org/10.1016/j.cej.2024.155591.
[20] J. Liu, Y. Hu, X. Li, C. Xiao, Y. Shi, Y. Chen, J. Cheng, X. Zhu, G. Wang, J. Xie, High-efficient degradation of chloroquine phosphate by oxygen doping MoS_2 co-catalytic Fenton reaction, J. Hazard. Mater. 458 (2023) 131894, https://doi.org/10.1016/j.jhazmat.2023.131894.
[21] Y. Su, L. Zhang, W. Wang, X. Li, Y. Zhang, D. Shao, Enhanced H_2 evolution based on ultrasound-assisted piezo-catalysis of modified MoS_2, J. Mater. Chem. A 6 (2018) 11909–11915, https://doi.org/10.1039/C8TA03208D.
[22] J. Xie, J. Zhang, S. Li, F. Grote, X. Zhang, H. Zhang, R. Wang, Y. Lei, B. Pan, Y. Xie, Controllable disorder engineering in oxygen-incorporated MoS_2 ultrathin nanosheets for efficient hydrogen evolution, J. Am. Chem. Soc. 135 (2013) 17881–17888, https://doi.org/10.1021/ja408329q.
[23] N. Luo, C. Chen, D. Yang, W. Hu, F. Dong, S defect-rich ultrathin 2D MoS_2: the role of S point-defects and S stripping-defects in the removal of Cr(VI) via synergistic adsorption and photocatalysis, Appl. Catal., B 299 (2021) 120664, https://doi.org/10.1016/j.apcatb.2021.120664.
[24] L. Li, R. Long, T. Bertolini, O.V. Prezhdo, Sulfur adatom and vacancy accelerate charge recombination in MoS_2 but by different mechanisms: time-domain ab initio analysis, Nano Lett. 17 (2017) 7962–7967, https://doi.org/10.1021/acs.nanolett.7b04374.
[25] Z. Li, S. Ma, Z. Jiao, Influence of S vacancy and O doping in MoS_2/GaN heterostructure on charge carrier dynamics: a time-domain ab initio study, Physica E 156 (2024) 115860, https://doi.org/10.1016/j.physe.2023.115860.
[26] J. Zhao, Y. Wang, H. Liu, R. Zhang, W. Jia, J. Zhang, Y. Sun, L. Peng, Understanding the role of dual zinc and indium vacancies in $ZnIn_2S_4$ for the visible-light-driven photocatalytic air-oxidation of 5-hydroxymethylfurfural, ACS Catal. 15 (2025) 3464–3474, https://doi.org/10.1021/acscatal.4c06911.
[27] B. Xie, L. Wang, H. Li, H. Huo, C. Cui, B. Sun, Y. Ma, J. Wang, G. Yin, P. Zuo, An interface-reinforced rhombohedral Prussian blue analogue in semi-solid state electrolyte for sodium-ion battery, Energy Storage Mater. 36 (2021) 99–107, https://doi.org/10.1016/j.ensm.2020.12.008.
[28] R. Lei, F. Gao, J. Yuan, C. Jiang, X. Fu, W. Feng, P. Liu, Free layer-dependent piezoelectricity of oxygen-doped MoS_2 for the enhanced piezocatalytic hydrogen evolution from pure water, Appl. Surf. Sci. 576 (2022) 151851, https://doi.org/10.1016/j.apsusc.2021.151851.
[29] J. Tang, Z. Wei, Q. Wang, Y. Wang, B. Han, X. Li, B. Huang, M. Liao, J. Liu, N. Li, Y. Zhao, C. Shen, Y. Guo, X. Bai, P. Gao, W. Yang, L. Chen, K. Wu, R. Yang, D. Shi, G. Zhang, In situ oxygen doping of monolayer MoS_2 for novel electronics, Small 16 (2020) 2004276, https://doi.org/10.1002/smll.202004276.
[30] L. Zeng, S. Chen, J. van der Zalm, X. Li, A. Chen, Sulfur vacancy-rich N-doped MoS_2 nanoflowers for highly boosting electrocatalytic N_2 fixation to NH_3 under ambient conditions, Chem. Commun. 55 (2019) 7386–7389, https://doi.org/10.1039/C9CC02607J.
[31] S. Wang, D. Zhang, B. Li, C. Zhang, Z. Du, H. Yin, X. Bi, S. Yang, Ultrastable in-plane 1T–2H MoS_2 heterostructures for enhanced hydrogen evolution reaction, Adv. Energy Mater. 8 (2018) 1801345, https://doi.org/10.1002/aenm.201801345.
[32] J. Qiu, D. Wang, Y. Chang, Q. Feng, Z. Liu, M. Pang, D. Meng, Y. Feng, C. Fan, Anchoring single-atom Cu on tubular g-C_3N_4 with defect engineering for enhanced Fenton-like reactions to efficiently degrade carbamazepine: performance and mechanism, Chem. Eng. J. 479 (2024) 147841, https://doi.org/10.1016/j.cej.2023.147841.
[33] S. Sun, Y. Hu, M. Xu, F. Cheng, H. Zhang, Z. Li, Photo-Fenton degradation of carbamazepine and ibuprofen by iron-based metal-organic framework under alkaline condition, J. Hazard. Mater. 424 (2022) 127698, https://doi.org/10.1016/j.jhazmat.2021.127698.
[34] S. Chen, X. Ding, J. Hu, H. Hou, J. Yang, Activation of peroxymonosulfate by iron phthalocyanine loaded on MoS_2 for efficient degradation of carbamazepine, Mater. Today Chem. 45 (2025) 102625, https://doi.org/10.1016/j.mtchem.2025.102625.
[35] L. Huang, Y. Ge, Z. Zheng, D. Wang, X. Wang, L. Yang, S. Fang, Co and S co-doped graphitic carbon nitride synergistically degrades carbamazepine in water with peroxymonosulfate, J. Water Process Eng. 71 (2025) 107220, https://doi.org/10.1016/j.jwpe.2025.107220.
[36] S. Lan, C. Yu, F. Sun, Y. Chen, D. Chen, W. Mai, M. Zhu, Tuning piezoelectric driven photocatalysis by La-doped magnetic $BiFeO_3$-based multiferroics for water purification, Nano Energy 93 (2022) 106792, https://doi.org/10.1016/j.nanoen.2021.106792.
[37] Y. Cheng, J. Chen, P. Wang, W. Liu, H. Che, X. Gao, B. Liu, Y. Ao, Interfacial engineering boosting the piezocatalytic performance of Z-scheme heterojunction for carbamazepine degradation: mechanism, degradation pathway and DFT calculation, Appl. Catal., B 317 (2022) 121793, https://doi.org/10.1016/j.apcatb.2022.121793.
[38] H.-Y. Lin, K.T. Le, P.-H. Chen, J.M. Wu, Systematic investigation of the piezocatalysis–adsorption duality of polymorphic MoS_2 nanoflowers, Appl. Catal., B 317 (2022) 121717, https://doi.org/10.1016/j.apcatb.2022.121717.
[39] M.-C. Lin, S.-N. Lai, K.T. Le, J.M. Wu, Self-powered photoelectrochemical quartz/TiO_2 microsystem through piezopotential sensitized photocatalytic process, Nano Energy 91 (2022) 106640, https://doi.org/10.1016/j.nanoen.2021.106640.
[40] J. Zhou, G. Fang, A. Pan, S. Liang, Oxygen-incorporated MoS_2 nanosheets with expanded interlayers for hydrogen evolution reaction and pseudocapacitor applications, ACS Appl. Mater. Interfaces 8 (2016) 33681–33689, https://doi.org/10.1021/acsami.6b11811.
[41] X. Ren, H. Wu, Y. Guo, H. Wei, H. Wu, H. Wang, Z. Lin, C. Xiong, H. Liu, L. Zhang, Z. Li, The impact of oxygen content in O-doped MoS_2 on the kinetics of polysulfide conversion in Li–S batteries, Small 20 (2024), https://doi.org/10.1002/smll.202312256.
[42] S. Song, Y. Li, Y. Shi, Y. Xu, Y. Niu, Oxygen-doped MoS_2 nanoflowers with sulfur vacancies as electrocatalyst for efficient hydrazine oxidation, J. Electroanal. Chem. 906 (2022) 115986, https://doi.org/10.1016/j.jelechem.2021.115986.
[43] X. Ning, D.-Z. Jia, S. Li, M. Khan, A. Hao, Oxygen-incorporated MoS_2 catalyst for remarkable enhancing piezocatalytic H_2 evolution and degradation of organic pollutant, Rare Met. 42 (2023), https://doi.org/10.1007/s12598-023-02363-4.
[44] Y. Shi, W. Zhang, J. Tan, T. Yan, Y. Jia, Z. Wang, Y. Tang, Q. Gao, Intercalation-driven defect-engineering of MoS_2 for catalytic transfer hydrogenation, Adv. Mater. Interfac. 9 (2022), https://doi.org/10.1002/admi.202200505.
[45] X. Wang, S. Li, Z. Yuan, Y. Sun, Z. Tang, X. Gao, H. Zhang, J. Li, S. Wang, D. Yang, J. Xie, Z. Yang, Y.-M. Yan, Optimizing electrocatalytic nitrogen reduction via interfacial electric field modulation: elevating d-band center in WS_2-WO_3 for enhanced intermediate adsorption, Angew. Chem. Int. Ed. 62 (2023) e202303794, https://doi.org/10.1002/anie.202303794.
[46] M. Liu, Y. Ning, M. Ren, X. Fu, X. Cui, D. Hou, Z. Wang, J. Cui, A. Lin, Internal electric field-modulated charge migration behavior in MoS_2/MIL-53(Fe) S-scheme heterojunction for boosting visible-light-driven photocatalytic chlorinated antibiotics degradation, Small 19 (2023) 2303876, https://doi.org/10.1002/smll.202303876.
[47] Z.J. Anqi Chen, Juntao Tang, Guipeng Yu, Photocatalytic production of hydrogen peroxide from covalent organic framework materials, Prog. Chem. 36 (2024) 357–366, https://doi.org/10.7536/PC230724.
[48] Q. Yang, J. Du, J. Li, Y. Wu, Y. Zhou, Y. Yang, D. Yang, H. He, Thermodynamic and kinetic influence of oxygen vacancies on the solar water oxidation reaction of α-Fe_2O_3 photoanodes, ACS Appl. Mater. Interfaces 12 (2020) 11625–11634, https://doi.org/10.1021/acsami.9b21622.
[49] Y. Deng, Z. Liu, A. Wang, D. Sun, Y. Chen, L. Yang, J. Pang, H. Li, H. Li, H. Liu, W. Zhou, Oxygen-incorporated MoX (X: s, Se or P) nanosheets via universal and controlled electrochemical anodic activation for enhanced hydrogen evolution activity, Nano Energy 62 (2019) 338–347, https://doi.org/10.1016/j.nanoen.2019.05.036.
[50] S. Karmakar, S. Biswas, P. Kumbhakar, A comparison of temperature dependent photoluminescence and photo-catalytic properties of different MoS_2 nanostructures, Appl. Surf. Sci. 455 (2018) 379–391, https://doi.org/10.1016/j.apsusc.2018.05.204.

[51] Y. Zheng, J. Yang, B. Gong, X. Zhang, J. Li, H. Zheng, G. Chen, C. Zhao, Hydraulic-driven piezo-activation of peroxymonosulfate for carbamazepine degradation with ultralow energy consumption, Chem. Eng. J. 441 (2022) 136116, https://doi.org/10.1016/j.cej.2022.136116.
[52] Q. Chen, H. Wu, J. Hu, Q. Tian, D. He, G. Lu, M. Zhu, Fe-metal organic framework converts mechanical energy with piezoelectric polarization to remove carbamazepine in water: efficiency, pathway and mechanism, Chem. Eng. J. 460 (2023) 141839, https://doi.org/10.1016/j.cej.2023.141839.
[53] E. Wu, Y. Yu, J. Hu, G. Ren, M. Zhu, Piezoelectric-channels in MoS_2-embedded polyvinylidene fluoride membrane to activate peroxymonosulfate in membrane filtration for wastewater reuse, J. Hazard. Mater. 458 (2023) 131885, https://doi.org/10.1016/j.jhazmat.2023.131885.
[54] Y. Zhao, F. Yang, H. Jiang, G. Gao, Piezoceramic membrane with built-in ultrasound for reactive oxygen species generation and synergistic vibration anti-fouling, Nat. Commun. 15 (2024) 4845, https://doi.org/10.1038/s41467-024-49266-1.
[55] S. Tu, Y. Guo, Y. Zhang, C. Hu, T. Zhang, T. Ma, H. Huang, Piezocatalysis and piezo-photocatalysis: catalysts classification and modification strategy, reaction mechanism, and practical application, Adv. Funct. Mater. 30 (2020), https://doi.org/10.1002/adfm.202005158.
[56] Y. Wang, Y. Xu, S. Dong, P. Wang, W. Chen, Z. Lu, D. Ye, B. Pan, D. Wu, C.D. Vecitis, G. Gao, Ultrasonic activation of inert poly(tetrafluoroethylene) enables piezocatalytic generation of reactive oxygen species, Nat. Commun. 12 (2021) 3508, https://doi.org/10.1038/s41467-021-23921-3.
[57] X. Fang, W. Qu, T. Qin, X. Hu, L. Chen, Z. Ma, X. Liu, X. Tang, Abatement of nitrogen oxides via selective catalytic reduction over Ce1–W1 atom-pair sites, Environ. Sci. Technol. 56 (2022) 6631–6638, https://doi.org/10.1021/acs.est.2c00482.
[58] R. Guo, L. Jin, H. Wang, R. Wang, X. Zhang, Y. Zhang, High-efficient U(VI) removal from organic wastewater through polarization electric field enhanced photocatalysis with In_2Se_3@Ag_3PO_4 heterojunction, J. Water Process Eng. 69 (2025) 106690, https://doi.org/10.1016/j.jwpe.2024.106690.
[59] Y. Liu, H.-Y. Xu, S. Komarneni, The piezoelectric and piezo-photoelectric effects: emerging strategies for catalytic performance enhancement of low-dimensional nanostructures, Appl. Catal., A 670 (2024) 119550, https://doi.org/10.1016/j.apcata.2023.119550.